ADVANCED OPTICAL MATERIALS
www.advopticalmat.de

A General Method for Direct Assembly of Single Nanocrystals

*Heyou Zhang, Yawei Liu, Arun Ashokan, Can Gao, Yue Dong, Calum Kinnear, Nicholas Kirkwood, Samantha Zaman, Fatemeh Maasoumi, Timothy D. James, Asaph Widmer-Cooper, Ann Roberts, and Paul Mulvaney**

Controlled nanocrystal assembly is a pre-requisite for incorporation of these materials into solid state devices. Many assembly methods have been investigated which target precise nanocrystal positioning, high process controllability, scalability, and universality. However, most methods are unable to achieve all of these goals. Here, surface templated electrophoretic deposition (STED) is presented as a potential assembly method for a wide variety of nanocrystals. Controlled positioning and deposition of a wide range of nanocrystals into arbitrary spatial arrangements – including gold nanocrystals of different shapes and sizes, magnetic nanocrystals, fluorescent organic nanoparticles, and semiconductor quantum dots – is demonstrated. Nanoparticles with diameters <10 nm are unable to be deposited due to their low surface charge and strong Brownian motion (low Péclet number). It is shown that this limit can be circumvented by forming clusters of nanocrystals or by silica coating nanocrystals to increase their effective size.

1. Introduction

A plethora of nanocrystals (NCs) have been synthesized over the last 30 years and these exhibit size-dependent properties including unusual plasmonic,[1,2] magnetic,[3] fluorescent,[4,5] catalytic,[6,7] analytic,[8] electronic,[9,10] and biological[11] responses. Nanocrystals may serve as plasmonic pixels[12] and as optical[13,14] and biological sensors. [15] They are also key components in various optical devices [16], metalenses,[17] drug delivery platforms,[18] tunable light emitting diodes, and other display technologies.[19] NCs have even played a significant role in the recent COVID-19 outbreak.[20,21] A common challenge in all of these proposed applications is the incorporation of single NCs into solid state device architectures.[22–24] Although top-down methods, such as physical or chemical vapor deposition provide a method for fabricating single NC arrays on a solid substrate, these approaches are still limited in terms of the range of materials which may be deposited.[25] Furthermore, these methods do not allow deposition of nanocrystals with complex morphologies such as core–shell nanocrystals.

A more promising approach is solution based single nanocrystal assembly. Broadly speaking, NC assembly may be driven either by chemical interactions (self-assembly) or by external forces (directed assembly). Strong progress has been made in crystallization of NCs into 2D and 3D superlattices via self-assembly and this has been reviewed extensively.[26–28] In such chemical self-assembly, interparticle forces are modified to shift the system from repulsive to weakly attractive. This can be achieved through temperature changes, pH changes, electrolyte addition, solvent evaporation, or addition of nonsolvents. The resultant superlattices exhibit properties which can be

H. Zhang, A. Ashokan, C. Gao, Y. Dong, N. Kirkwood, S. Zaman, F. Maasoumi, P. Mulvaney
ARC Centre of Excellence in Exciton Science
School of Chemistry
University of Melbourne
Parkville, Victoria 3010, Australia
E-mail: mulvaney@unimelb.edu.au

Y. Liu, A. Widmer-Cooper
ARC Centre of Excellence in Exciton Science
School of Chemistry
University of Sydney
Sydney, New South Wales 2006, Australia

The ORCID identification number(s) for the author(s) of this article can be found under https://doi.org/10.1002/adom.202200179.

DOI: 10.1002/adom.202200179

Y. Dong
Department of Nanostructural Materials
Leibniz-Institut für Polymerforschung Dresden e.V.
01069 Dresden, Germany

C. Kinnear
CSL Limited
Parkville, Victoria 3010, Australia

T. D. James
Reserve Bank of Australia
Craigieburn, Victoria 3064, Australia

A. Widmer-Cooper
The University of Sydney Nano Institute
University of Sydney
Sydney, New South Wales 2006, Australia

A. Roberts
ARC Centre of Excellence for Transformative Meta-Optical Systems
School of Physics
University of Melbourne
Parkville, Victoria 3010, Australia

tuned through variation of the interparticle spacing. However, the geometry of the final structure of the composite material is predetermined by the nature of the forces between the NCs. While this can be controlled to some extent, arbitrary geometries cannot be attained.

Direct assembly offers some key advantages over chemical self-assembly. Since an external force is applied, the NCs can remain colloidally stable. This is more practical than destabilization of the NCs to drive assembly. The external force can be modulated in time and space. However, the external force will generally drive the NCs to assemble into a superstructure in the same way as chemical self-assembly unless the forces are used to drive the single NCs into spatially well-defined locations. Hence the solution to this problem is surface templating, that is, the surface or substrate must be prepatterned to steer individual NCs to deposit into preordained positions. The second step is identification of suitable ways to achieve chemical or physical contrast on the surface.[25] For example, in capillary force assembly (CFA), NCs are "pushed" into pre-designed surface cavities by the capillary forces at the moving solid-liquid-air interface.[29–31] CFA can be used to assemble NCs with nanometer precision[32] and with predictable orientation.[33,34] Another important method is electrostatic assembly, which is based on the electrostatic interaction between the particle and substrate.[35–37] The substrate is pre-functionalized in such a way that an electrostatic contrast is generated, which enables NCs of opposite charge to be selectively adsorbed.[38,39] Optical printing is yet another effective method for single particle assembly and positioning. It works best for micron-scale particles. However, with the implementation of higher power, focused laser sources, optical printing also offers the ability to manipulate NCs at the single particle level, that is, the laser can function as a single particle optical tweezers.[40–42] DNA-assisted chemical assembly is based on the specific DNA binding between DNA modified NCs and a surface spatially patterned with the complementary DNA strand. This method can be used to construct quite complex nanostructures.[43–45] All of these methods suffer from some limitations. For example optical printing is quite generic but is relatively slow and offers only micron level spatial patterning. DNA based assembly is expensive to implement, while CFA is difficult to scale up due to its sensitivity to surface roughness. It is also worth mentioning template-assisted self-assembly.[46,47] This method is a combination of colloidal self-assembly and directed assembly. The colloidal self-assembly depends on controlling the particle-particle interactions in the colloid in order to form a complex nanoparticle structure, such as a dimer, trimer, or super-lattice and this is then deposited onto a suitably templated substrate.

Here we focus on an alternative method—surface templated electrophoretic deposition (STED). It is based on the conventional electrophoretic deposition (EPD) of charged NCs under the influence of an applied electric field.[48–50] However, deposition is carried out using a nanoscale, prepatterned, conducting substrate. The primary requirement for successful single NC deposition is that the particles be uniformly charged. However, monodispersity is also important because electrophoretic forces are size-dependent and deposition will favor those particles in a NC solution with the highest electrophoretic mobility. Electrophoresis is also easier to carry out in solvents of high dielectric constant. In principle, STED can be applied to all kinds of NCs, provided they have a well-defined shape and size and can sustain a well-defined surface charge.[51]

In early reports of conventional EPD, thin films of particles such as cadmium selenide (CdSe),[52–54] carbon nanomaterials,[55,56] or metal oxides[57–59] were created by continuous EPD. In contrast the focus here is on deposition and positioning of single NCs. To date, there have been few studies of NC assembly at the single particle level, with the pioneering work by Wolf and colleagues[60,61] as well as studies on polystyrene particle deposition being notable exceptions.[62–65]

In this article we demonstrate the versatility of STED by creating arrays of different types of NCs. Gold NCs with different shapes and sizes, magnetic NCs, organic fluorescent nanoparticles as well as semiconductor quantum dots are all investigated. Square arrays are used for their ease of analysis but the process can be applied to form arbitrary 2D patterns. We also discuss the effect of particle size during STED assembly and propose two approaches to overcome the lower particle size limit.

2. Results

Figure 1 shows scaning electron microscopy (SEM) images of gold NCs with different shapes (a–c) as well as gold nanospheres with different sizes (d–f). Each figure shows a 3 × 3 single particle array with 5 μm particle-to-particle spacing. A high magnification inset in each figure shows an image of individual gold NCs in the respective arrays. SEM confirms that single NCs are deposited in each case.

In Figure 1a, we used a template with rectangular cavities (with lengths of 120 nm and widths of 60 nm) to assemble gold nanorods (with average lengths of 110 nm and widths of 50 nm) into arrays. The final orientation of the individual rods is controlled by the orientation of the template. Gold nanocubes (with average lengths of 44 nm) can also be assembled into an array of square cavities (with lateral dimensions of 50 nm). In Figure 1b and Figure S2, Supporting Information, we show that the orientation of the gold nanocubes within the cavities matches the orientation of the square cavities. The cavities are only 6 nm larger than the mean cube diameter, which reduces the probability of deposition at an angle within the cavities. Despite the small size mismatch, deposition is highly efficient. While steric factors clearly determine the packing of NCs, it is possible that electrostatic forces still play a role. Inside a cavity, there is a complicated electric field distribution due to the presence of both charged particles and electrolytes. The PMMA based cavity walls may also be charged due to the presence of surface carboxyl groups. Therefore, electrical forces may help determine the final orientation of particles and may also play a role in ensuring there is just one particle deposited per cavity. Gold nano-octahedra (with average diameters of 110 nm) were also deposited onto a template with square cavities (with diameters of 130 nm). This resulted in single particle arrays as expected (Figure 1c). However, we did not find any preferred orientation for the gold nano-octahedra. The inset to Figure 1c shows a single, hexagonally shaped particle, which is one of the projections of the octahedron. Other projections of the octahedron, such as square and rhombus, were also observed as shown in Figure S3, Supporting Information.

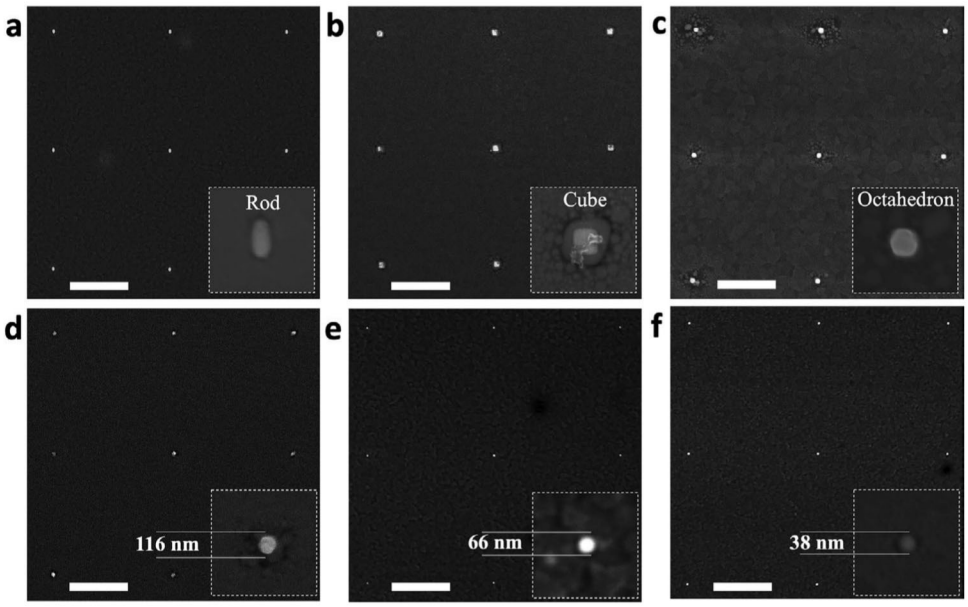

Figure 1. Scanning electron microscopy images of gold NC arrays following STED onto EBL-patterned, PMMA-coated ITO glass. a) Gold nanorods, b) gold nanocubes and c) gold nano-octahedra; gold spheres with diameters of: d) 116, e) 66, and f) 38 nm. (Scale bar: 2 µm)

Gold nanospheres of various sizes can be assembled into single NC arrays as shown in Figure 1d–f. We used gold nanospheres (with an average diameters of 116, 66, and 38 nm). Three templates with corresponding square cavities (with sizes of 130, 70, and 50 nm) were used with the corresponding gold nanosphere solutions. Cavities were filled with only one particle, since the size of each cavity was only slightly larger than the average size of the nanospheres. It is worth noting that during the assembly of the three different sizes of gold nanospheres, the solution conditions were generally the same, that is, [NaCl] = 0.5 mM, t = 10 s. However, a different applied DC potential, Φ, was used in each case during assembly. Specifically, −3 V was applied for the assembly of 116 nm gold nanospheres, −3.5 V for the assembly of 66 nm gold nanospheres, and −4 V for the assembly of 38 nm gold nanospheres.

Metal oxide NCs and organic NCs were also used to test the versatility of the method. We prepared magnetite NCs (Fe_3O_4) based on a modified hydrothermal method, previously reported.[66] The resultant superparamagnetic NCs were formed from clusters of Fe_3O_4 nuclei which were initially stabilized by poly(4-styrenesulfonic acid-co-maleic acid) (PSSMA). **Figure 2**a shows a dark field scattering image collected from a 60 × 60 array of Fe_3O_4 NCs. Due to the 5 µm particle-to-particle spacing, we could directly observe the Rayleigh scattering from each individual particle through a dark field microscope. We found that the scattered light from magnetite NCs exhibited a surprisingly uniform yellow color. The mean particle size was found to be ≈200 nm (Figure 2b). Atomic force microscopy (AFM) and magnetic force microscopy (MFM) were used to further characterise the magnetic properties of the arrays, as shown in Figure 2c,d. Figure 2c is an AFM topography image of a 3 × 3 section of the Fe_3O_4 NC array from Figure 2a. The template had a PMMA thickness of 100 nm and square cavity size of 210 nm. Therefore, the magnetite particles protruded >80 nm above the PMMA layer and could be readily imaged by AFM. Figure 2d shows an MFM image for the same area from Figure 2c. The MFM cantilever was magnetized using a neodymium magnet. For MFM measurements, the cantilever was raised 30 nm compared to the previous topography mode for recording the magnetic interaction between the Fe_3O_4 NCs and the cantilever tip. Hence, during MFM measurements, the cantilever trajectory followed the topography profile of the substrate. The height of the nanoparticles and the surface roughness did not affect the MFM data. Comparing Figure 2c,d, a magnetic attraction was detected at every spot where a Fe_3O_4 NC was located, due to interaction with the superparamagnetic Fe_3O_4 NCs.

To demonstrate STED assembly of organic fluorescent nanoparticles, we prepared aggregates of 9,10-bis(phenylethynyl) anthracene (BPEA) as our target, whose molecular structure is shown in Figure 2g. BPEA is a commonly used, fluorescent anthracene derivative, which can be easily prepared in the form of nanoparticles in aqueous solution.[67] The BPEA aqueous colloid was stabilized by sodium dodecyl sulfate (SDS) and displayed a zeta potential ζ = −48 mV ±2 mV and diameter D = 117 nm (measured by dynamic light scattering [DLS]). In addition, the BPEA fluorescence allowed us to image the particles using a modified wide field microscope. The microscope setup is illustrated in Figure S4, Supporting Information. In the case of the BPEA organic nanoparticle array, we used a blue laser at 375 nm as the excitation source and a 500 nm long pass filter when capturing the fluorescence. A typical fluorescence microscope image of the BPEA array is shown in Figure 2e. As with the arrays discussed above, we designed the particle-to-particle distance to be 5 µm in order to be able to visualise each particle under the microscope. Because the average size of the BPEA nanoparticles was 117 nm (Figure 2f), we used a template with cavity sizes of 130 nm. After STED, a clear and uniform green emitting array was observed, which indicated the deposition of BPEA nanoparticles. However, we could also clearly see that there

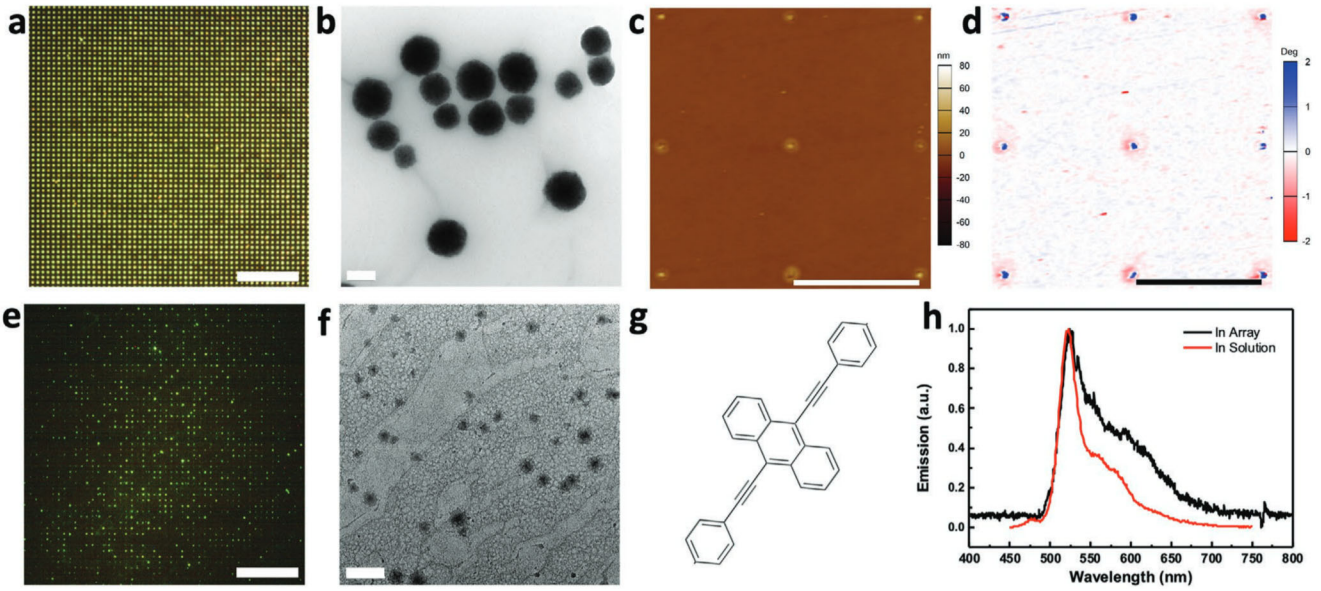

Figure 2. a–d) EPD assembly of Fe_3O_4 magnetic NCs and e–h) fluorescent organic NCs. a) Dark field microscope image of Fe_3O_4 NC arrays. (Scale bar: 50 µm). b) TEM image of Fe_3O_4 NCs. (Scale bar: 200 nm). c) AFM topography of the Fe_3O_4 NC arrays (scale bar: 5 µm), and d) corresponding magnetic force microscope (MFM) image over the same region as (c). (Scale bar: 5 µm). e) Wide field microscope image of the 9,10-bis(phenylethynyl) anthracene (BPEA) NC array. (Scale bar: 50 µm). f) TEM image of the BPEA nanoparticles prepared in aqueous solution. (Scale bar: 200 nm). g) Molecular structure of the BPEA monomer. h) Emission spectrum of the BPEA nanoparticles in aqueous solution (red) and in a single cavity of the array shown in (e) (black).

were some missing spots in the array where no fluorescence could be observed. Imperfect arrays were likely caused by: 1) fluorescence quenching of dye aggregates in the cavities,[68] 2) fluorescence quenching due to electrostatic charging by the ITO electrode,[69] or 3) incomplete deposition of BPEA nanoparticles into the cavities. The ensemble emission spectrum of BPEA nanoparticles in aqueous solution (red line) together with the single particle emission spectrum (black line) are shown in Figure 2h. Both spectra evinced a strong emission peak at 525 nm which corresponded to the observed green color. Furthermore, both spectra also exhibited the signature shoulder peak of the BPEA nanoparticle[70] around 570 to 620 nm. This demonstrated that the BPEA nanoparticles had been successfully deposited into the array via STED. However, compared to the BPEA nanoparticles in aqueous solution, the deposited BPEA particle spectrum also showed a small red shift which may have been due to the changing polarity within the cavity.

Of greater interest is the STED assembly of semiconductor NCs or QDs. We selected CdSe/CdS/ZnS quantum dots as our assembly target due to their high quantum yield and photostability.[71] Phase transfer of the QDs from their native organic solvent (hexane) to water was achieved by ligand exchange with 11-mercaptoundecanoic acid (MUA) (**Figure 3**a). There was a negligible PL shift following phase transfer and minor loss of PL intensity (see Figure S5b, Supporting Information). However, despite varying the experimental parameters considerably, we were unable to find deposition conditions that would enable large scale, uniform STED of single QDs.

Because the QDs cannot be made any larger without changing their optical properties, we used another approach to increase the effective size of the QDs—collecting multiple QDs within a polymer shell to form a cluster with a larger hydrodynamic size. The basic coating procedure is shown in Figure 3a. We used a positively charged polyelectrolyte, poly-diallyldimethylammonium chloride (pDADMAC), to coat the negatively charged QD-MUA NCs.[72] The size of the pDADMAC coated QDs (QD-MUA-pDADMAC) was measured to be 85 nm ± 10 nm by DLS and the zeta potential was measured to be +42 mV ± 2 mV. Using the same coating procedure, the final size of the QD clusters could be controlled by tuning the QD-MUA concentration during coating, as shown in Figure S5a, Supporting Information. Following pDADMAC coating, there was a small red shift of the emission spectrum (from 611 to 619 nm) due to QD aggregation within the polymer shell as shown in Figure S5b,c, Supporting Information. However, the increase in hydrodynamic size after polymer coating facilitated STED assembly. Figure S5e, Supporting Information presents a set of wide field microscopy images of STED assembled QD-MUA-pDADMAC clusters. We employed an ITO-PMMA template with different cavity sizes, ranging from 30 nm to 500 nm. As evident from Figure S5e, Supporting Information, the cavity filling percentage generally increased with an increase in the cavity size. When the cavity sizes were 30 and 50 nm, the QD filling rate in the array was very low since the average size of the QD-MUA-pDADMAC NCs was around 85 nm, which was larger than the cavity size. When the cavity sizes were 70 and 90 nm, the observed cavity filling percentage was still relatively low, but some array patterns began to emerge. This was a result of the inhomogeneous size distribution of the polymer coated QD clusters. When the cavity size reached 110 nm, the cavity filling efficiency increased drastically and a clear array was observed. Increasing the cavity size further, from 130 to 500 nm, allowed close to 99% filling of the wells to be achieved.

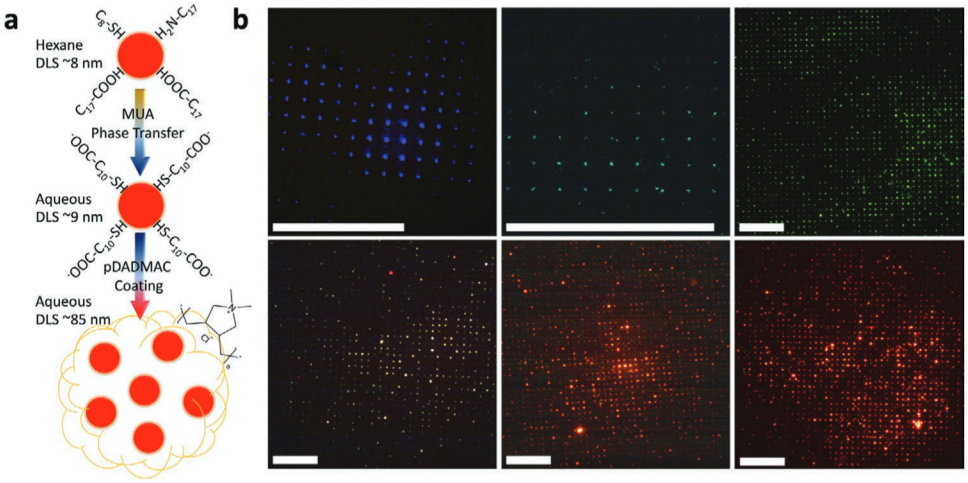

Figure 3. The results of STED assembly of polymer coated QD clusters. a) Scheme illustrating the process of QD phase transfer and pDADMAC polymer coating. The phase transfer process was carried out by ligand exchange with MUA. The MUA coating resulted in a zeta potential of −82 mV ± 2 mV (0.5 mM NaCl), and DLS yielded a size of ≈9 nm ± 2 nm in diameter. The QD-MUA NCs were then coated with pDADMAC (QD-MUA-pDADMAC) which resulted in a positive zeta potential of +43 mV ± 2 mV (0.5 mM NaCl), while DLS yielded a size of ≈85 nm ± 10 nm. b) A set of wide field images of arrays of pDADMAC coated QD clusters which exhibited colors ranging from violet, cyan, and green through to yellow, orange, and red. (Scale bar: 40 μm). (Brightness and contrast have been slightly adjusted for better presentation.)

Based on the approach of coating small QDs into bigger clusters by polyelectrolyte coating, we expanded the EPD assembly to QDs with different photoluminescence (PL) properties. Figure 3b shows a set of wide field fluorescence microscopy images of QD arrays with different PL colors. All six samples were phase transferred using MUA followed by polymer coating with pDADMAC, as described in Experimental Section. (Figure S6a, Supporting Information shows a photograph of QDs of various sizes in aqueous solution under illumination by a UV lamp.) Under the STED conditions used, that is, $\Phi = -3.5$ V, [NaCl] = 0.5 mM and t = 10 s, we were able to successfully assemble arrays using all six samples. The corresponding single cavity emission spectra are presented in Figure S6b, Supporting Information. The emission peaks of the samples are: 425 nm for violet QDs, 510 nm for cyan, 540 nm for green, 561 nm for yellow, 606 nm for orange and 645 nm for red QDs. Note that the wide field emission spectra were from a cluster of QDs inside each cavity. They generally exhibited broader peaks than the corresponding solution spectra due to QD aggregation but were much brighter than single QDs. The clusters themselves could be readily patterned into higher order structures with good fidelity. Figure S7, Supporting Information shows a "star" shape pattern and the word "coupling" created by assembling QDs. The size of the "star" pattern was 40 μm in diameter. The width of each trench was 150 nm which was sufficient for polymer coated QDs clusters to deposit. For the word "coupling," the total length of the lettering was 200 μm. The width of each trench was 10 μm. Importantly, there was little evidence for nonspecific binding of QDs outside the wells.

Although polyelectrolyte coating of QDs enabled us to bypass the size limit of the EPD assembly method, the resultant arrays were not at the single particle level. The cluster of QDs created by polymer encapsulation exhibited red-shifted emission peaks and PL broadening, as well as decreased colloidal stability. A better embodiment could be achieved via silica encapsulation. Silica coating of semiconductor NCs was originally reported by Giersig and Liz–Marzán and was improved in various subsequent studies.[73] **Figure 4**a presents transmission electron microscopy (TEM) images of SiO_2 coated QDs prepared using a protocol outlined previously.[74] The average size of the QDs was 8 nm. After the SiO_2 coating, the total size of the core–shell NCs increased to ≈40 nm in diameter. With such a size increase, we were able to carry out single particle STED when: $\Phi = -4$ V, [NaCl] = 0.5 mM and t = 10 s. The results of STED assembly of

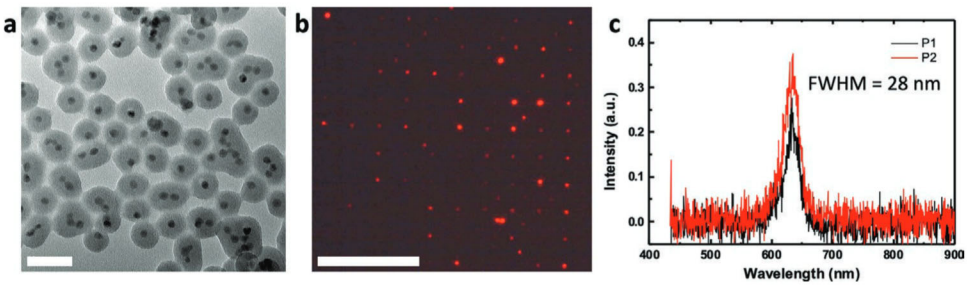

Figure 4. The results of STED assembly for SiO_2 coated QDs. a) TEM characterization of QD@SiO_2. (Scale bar: 50 nm). b) Wide field image of the STED assembled QD@SiO_2 array. (Scale bar: 20 μm). c) Emission spectra of two individual QD@SiO_2 particles in the assembled array.

QD@SiO_2 are shown in Figure 4b,c. Figure 4b is a wide field image of an array of QD@SiO_2 particles and Figure 4c presents the corresponding single particle emission spectra for two particles selected from less bright dots in Figure 4b. The full widths at half maximum (FWHM) of the two emission peaks were 28 nm, consistent with single QD emission. We also observed the blinking of single QDs within cavities as shown in the supporting video. This also provided evidence that a single QD was deposited into each cavity in the array. However, during SiO_2 coating, it was still possible to have multiple QDs within one SiO_2 shell as is evident from Figure 4a. This resulted in a number of QDs being deposited into the arrays, as is shown in Figure 4b. Note that, the contrast and brightness in Figure 4b and supporting video were increased slightly in order to better visualize the single QD arrays.

3. Discussion

We have demonstrated that STED assembly of numerous different kinds of NC is possible. Particles may be conducting or insulating, magnetic, or nonmagnetic and may adopt a range of morphologies. However, particles with smaller sizes generally require a higher applied potential to drive the assembly process. Since the applied potential cannot be increased indefinitely without causing electrolysis of the solvent, damage to the NCs or corrosion of the template, single NCs with sub-10 nm sizes cannot be deposited directly via the STED method without artificially increasing the NC size.

The size limitation is more or less determined by the competing effects of the electrical double layer around the NCs and Brownian motion. According to electrical double layer theory, all surface charges on a charged particle in the solution are screened by a diffuse layer of ions, which has the same absolute charge but opposite sign with respect to that of the surface charge. When an external electric field is applied, the charged particle moves under the electrostatic force acting on the bare charge of the particle, which is balanced by the hydrodynamic friction force at the particle–liquid interface, and other forces caused by the ion movement and deformation of the diffuse layer.[75] The electrostatic force on the charged particle from the external electric field, that is, the driving force for the electrophoretic mobility ($F_E = |\vec{F_E}|$), is given by

$$F_E = q_{NP}E \tag{1}$$

where q_{NP} is the total surface charge on the particle and $E = |\vec{E}|$ is the strength of the electric field applied to the particle. Assuming a spherical particle, the total surface charge on the particle can be written as

$$q_{NP} = 4\pi R^2 \rho_q \tag{2}$$

where R is the hydrodynamic radius of the particle (defined by the position of the slip plane where the ζ-potential is defined) and ρ_q is the surface charge density on the slip plane. The surface charge density on the slip plane of a particle in aqueous solution can be further obtained from the experimentally accessible ζ-potential. The surface charge density and zeta potential are related via[76]

$$\rho_q = \frac{2\varepsilon_0\varepsilon_r\kappa k_B T}{e}\sinh\left(\frac{e\zeta}{2k_BT}\right)\left[1+\frac{1}{\kappa R}\frac{2}{\cosh^2\left(\frac{e\zeta}{4k_BT}\right)}+\frac{1}{(\kappa R)^2}\frac{8\ln\left[\cosh\left(\frac{e\zeta}{4k_BT}\right)\right]}{\sinh^2\left(\frac{e\zeta}{2k_BT}\right)}\right]^{1/2} \tag{3}$$

where ε_0 is permittivity of free space, ε_r is relative permittivity, κ^{-1} is the double layer thickness, k_B is Boltzmann's constant, T is the absolute temperature, and e is the elementary charge. The double layer thickness is given by[48,77]

$$\kappa^{-1} = \left(\frac{\varepsilon_0\varepsilon_r k_B T}{2cz^2e^2}\right)^{\frac{1}{2}} \tag{4}$$

where c is the electrolyte concentration and z is the (symmetrical) ion valence.

In the presence of an experimentally realistic electric field, a minimum particle charge is needed to drive electrophoretic

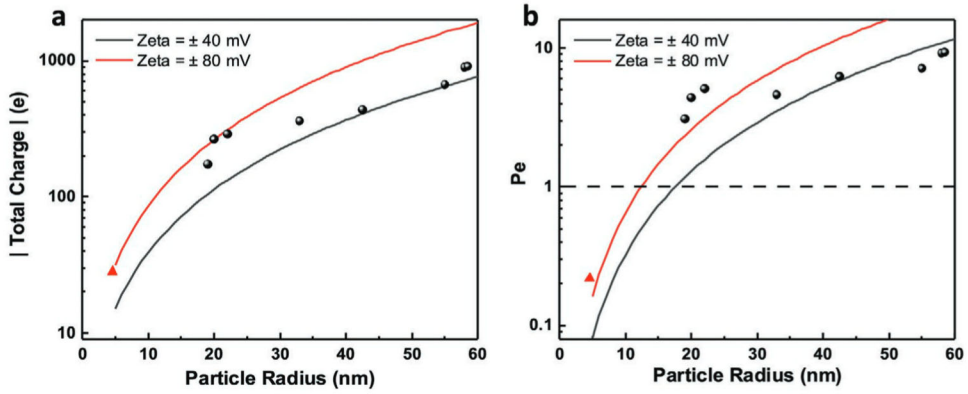

Figure 5. Effect of particle size on transport during STED. a) Plot of total charge on single NCs as a function of particle radius for two different zeta potentials using Equations (2)–(4). b) Plot of the calculated Péclet number (defined as the ratio of the electrophoretic transport rate to the diffusional transfer rate) as a function of particle radius, calculated using Equation (6). Conditions used: T = 298 K, [NaCl] = 0.5 mM, Φ = 3.5 V. Also shown are values for the NCs used in the experiments, based on the values in Table 1. The QD-MUA NCs are represented by red triangles while the other NCs are plotted using black spheres.

Table 1. Nanocrystal parameters and STED assembly conditions used in the experiments.

Sample name	Particle radius	Zeta potential	Applied potential	Calculated electric field	Total charge	Peclet number
Fe_3O_4	100 nm	+60.4 ± 0.8 mV	−3 V	8.9 V mm^{-1}	3314.7 *e*	34.2
BPEA	58.5 nm	−48.2 ± 2.1 mV	+3 V		906.5 *e*	9.3
Au spheres 116	58 nm	+48.3 ± 2.5 mV	−3 V		894.5 *e*	9.2
Au octahedra	55 nm	+41.2 ± 2.4 mV	−3 V		672.5 *e*	7.1
QD-MUA-pDADMAC	42.5 nm	+42.5 ± 2.4 mV	−3.5 V	12.7 V mm^{-1}	437.7 *e*	6.2
Au spheres 66	33 nm	+52.7 ± 1.8 mV	−3.5 V		360.9 *e*	4.6
Au cubes	22 nm	+76.4 ± 3.3 mV	−4 V	21.6 V mm^{-1}	289.7 *e*	5.1
QD@SiO_2	20 nm	+80.2 ± 1.6 mV	−4 V		263.6 *e*	4.4
Au spheres 38	19 nm	+62.6 ± 2.3 mV	−4 V		174.2 *e*	3.1
QD-MUA	4.5 nm	−82.3 ± 1.8 mV	+4 V	21.6 V mm^{-1}	28.3 *e*	0.22

deposition. Using Equations (2)–(4), we have calculated the value of $|q_{NP}|$ as a function of R under common experimental conditions (i.e., T = 298 K and [NaCl] =0.5 mM) and for two typical ζ-potentials (i.e., ±40 and ±80 mV) in our experiments; the results are given in **Figure 5**a. The absolute total surface charge increases as the magnitude of the ζ-potential increases. However, even though the small QD-MUA particle (ζ = –82.3 mV, D = 9 nm, $q_{NP} \approx 28\ e$) has a higher absolute ζ-potential than the large QD-MUA-pDADMAC particle (ζ = 42.5 mV, D = 85 nm, $q_{NP} \approx 438\ e$), the former has a much lower absolute surface charge compared to the latter, due to the huge differences in surface area. This means the larger QD-MUA-pDADMAC particles experience a larger driving force from the applied electric field and are thus more likely to undergo STED. The estimated electrostatic charge on the NCs used in our experiments are tabulated in **Table 1**) and plotted in Figure 5a as a function of the particle radius. Compared to the QD-MUA NCs (red triangle) the rest of the samples (black spheres) in our experiments carry a much higher total charge. The gold nanospheres with a diameter of 38 nm carry the second lowest total charge (174 *e*). To impose the same driving force on the QD-MUA particles, we would need to apply a approximately six times higher electric field, which would result in damage to the PMMA template and excessive electrolysis, and interfere with the STED process.

Further insights can be obtained by analyzing the movement of the particles during the STED process. Various analytic expressions have been introduced to calculate electrophoretic mobilities (μ) depending on the size of the particles. Based on Henry's equation, the electrophoretic mobility is given by,

$$\mu = \frac{v}{E} = \frac{2\varepsilon_0\varepsilon_r\zeta}{3\eta} f(\kappa r) \tag{5}$$

where v is the velocity of the particle, η is the viscosity of the solvent and $f(\kappa r)$ is the Henry's function. Within the Smoluchowski limit, Henry's function can be simplified to $f(\kappa r)$ = 1.5.[78,79] Within the nanoscale regime, the movement of particles is also significantly influenced by Brownian motion. In order to achieve efficient STED, electrophoretic motion needs to be considerably more effective than the Brownian motion at transporting the NCs. This can be quantified via the Péclet number (*Pe*). In the case of electrophoresis, we can define the Péclet number as follows:

$$Pe = \frac{vL}{D_t} = \frac{\frac{\varepsilon_0\varepsilon_r\zeta}{\eta}\cdot E\cdot 2R}{\frac{k_BT}{6\pi\eta R}} = 12\frac{\varepsilon_0\varepsilon_r\pi}{k_BT}\zeta ER^2 \tag{6}$$

where L is the characteristic length and is approximately equal to the diameter of the particle (i.e., $L \approx 2R$), D_t is the translational diffusion coefficient of the particle and is given by the Stokes–Einstein equation (i.e., $D_t = k_BT/(6\pi\eta R)$ with η is the dynamic viscosity of the solvent).

To compute the *Pe* number for particles under a given experimental condition, knowledge of the electric field E that they experience is required. Because the system has a significant electric current during the EPD process, here we determine the value of E by using Ohm's law (i.e., $J = \sigma E$, where $J = |\vec{J}|$ is the current density, σ is the conductivity of the solution and $E = |\vec{E}|$ is the electric field). The current density can be obtained from $J = I/A$ where I is the actual current recorded in the experiments and A is the effective surface area of the electrode based on the exposed area of the ITO-PMMA template (see Figure S6, Supporting Information, $A \approx 1.83 \times 10^{-8}$ m^2). Due to the fixed electrolyte concentration in all experiments, the currents recorded are relatively stable for each applied potential and $I \approx$ 14, 20, and 34 μA at Φ = 3, 3.5, and 4 V, respectively.

In general, when $Pe < 1$, Brownian motion dominates, leading to extremely slow deposition, while for $Pe > 1$, effective assembly of NCs occurs. These results are consistent with the analysis by Solomon et al.[65] We plotted the value of *Pe* as a function of R for the experimental conditions used here (i.e., T = 298 K, [NaCl] = 0.5 mM, Φ = 3.5 V, and I = 20 μA) for two typical ζ-potentials of NCs (i.e., ±40 mV (black curve) and ±80 mV (red curve)) in our experiments, and the results are shown in Figure 5b. We can see that, when $|\zeta|$ = 40 and 80 mV, $Pe < 1$ for particle size R < 18 nm and <13 nm, respectively, and Brownian motion dominates, which prevents electrophoretic deposition from occurring. Conversely, $Pe > 1$ for larger particles, and the electrophoretic motion dominates, which results in efficient STED assembly. We have also estimated the Péclet number for the samples in our experiments. These are

summarized in Table 1 and indicated by symbols in Figure 5b. The large particles in our experiments (black spheres) always have $Pe > 1$, meaning that electrophoretic motion can drive these NCs toward the substrate. However, the smaller QD-MUA particles (red triangles) have $Pe \approx 0.2$ under our experimental conditions, which explains why they do not assemble. Moreover, since Pe is proportional to the square of the particle radius R^2 but only to the first power of the ζ-potential (Equation (6)), increasing the size of the QDs using polyelectrolyte coatings or SiO_2 shells can be an efficient way to achieve successful EPD assembly, even if the coating process reduces the ζ-potential.

Note that the results above are calculated within the Smoluchowski limit ($\kappa r \gg 1$). However, as the particle size decreases below ≈13 nm (corresponding to $\kappa r = 1$), the Smoluchowski limit breaks down and the Henry's function decreases from 1.5 toward its lower limit of 1 when $\kappa r \ll 1$. This implies that the actual mobility and the corresponding Péclet numbers for smaller particles can be even lower than calculated above.

4. Conclusions

In summary, we have demonstrated that STED offers a versatile mechanism for positioning large numbers of single NCs with nanometer precision. The method is scalable, rapid, and will work for a wide variety of materials. The lower size limit is due to the increasing difficulty of overcoming Brownian motion. One way to circumvent this limit is by using a poly-electrolyte coating or SiO_2 shell to artificially increase the NC size. This raises the intriguing possibility of assembling single molecule arrays. The effective Péclet number of single molecules in solution is much less than one, which may render it difficult to carry out directly via STED. One possibility is that a single molecule (including proteins or oligonucleotides) could be adsorbed onto a NC or embedded within a polymeric substrate particle and thus be deposited via STED.

5. Experimental Section

Gold Nanorods: Gold nanorods were synthesized using the binary surfactant method.[80] The resulting gold nanorods were washed to remove excess CTAB by centrifugation at 2000 rcf for 10 min. Then, the precipitated gold nanorods were dispersed in water resulting a concentration of 50 µg mL^{-1}. To overcoat the gold nanorods with pDADMAC, 2 mL of washed gold nanorods were mixed with 1 mL of 10 mM NaCl solution under mild stirring. Meanwhile 2 mL of 1% polystyrene sulfonate (PSS) solution was mixed with 1 mL of 10 mM NaCl solution under mild stirring as well. The gold nanorod mixture was then added to the PSS mixture dropwise under vigorous stirring. After 5 min, the solution was left standing for at least 30 min. then it was centrifuged at 1500 rcf for 10 min to remove excess PSS. Finally, the precipitated gold nanorods were then redispersed in 2 mL water. The same step was repeated but replacing PSS with 1% poly(diallyldimethylammonium chloride) (pDADMAC) in order to carry out coating with the cationic polymer.

Gold Nanocubes: Gold nanocubes were synthesized using literature protocols.[81] The resulting gold nanocubes were washed to remove excess CTBA by centrifugation at 2500 rcf for 5 min. The pDADMAC coating step was the same as the one described above for coating gold nanorods.

Gold Nano-octahedra: Gold nano-octahedra were synthesized using published protocols.[82] The gold nano-octahedra were synthesized with a pDADMAC coating, so no further coating step was required.

Gold Nanospheres: Gold nanospheres with different sizes were synthesized using published procedures.[83] The resulting gold nanospheres were coated by pDADMAC using the same steps described for gold nanorods. However, because the synthesized gold nanospheres were stabilized by negatively charged trisodium citrate, the initial PSS coating step was not required.

Fe_3O_4 Nanocrystals: Fe_3O_4 nanocrystals were synthesized using published methods.[66] The Fe_3O_4 nanocrystals had a PSSMA coating, and displayed a zeta potential of $\zeta = -52$ mV ± 1 mV. They were further coated by pDADMAC using the steps described above in the gold nanorod section. The final pDADMAC coated Fe_3O_4 nanocrystals had a zeta potential of $\zeta = +60$ mV ± 1 mV.

BPEA Organic Nanocrystals: BPEA organic nanocrystals were synthesized based on literature procedures.[67] Briefly, BPEA in tetrahydrofuran (1 mM, 1 mL) was added dropwise into 6 mL of 10 mM sodium SDS aqueous solution. The mixture was stirred vigorously at room temperature for 10 min and aged overnight. The resulting solution was then washed by centrifuging at 5000 rcf for 20 min three times and the purified colloid was then redispersed in 5 mL water.

Quantum Dots: Red, orange, yellow, and green quantum dots were synthesized using standard protocols.[71] The final nanocrystals were CdSe/CdS/ZnS core–shell nanocrystals with tunable CdSe core sizes. Violet and cyan emitting quantum dots were synthesized via a second published protocol.[16,84] They were CdZnS/ZnS core–shell nanocrystals with controlled Cd to Zn ratios for tuning the PL wavelength.

Quantum Dots Phase Transfer: The synthesized QDs were phase transferred by adopting a published procedure.[85] The QD solutions were first precipitated with an anti-solvent (methanol or acetone), then centrifuged at 3000 rcf to remove the solvent. They were redispersed in 10 mL of hexane. Meanwhile, 0.2 g KOH along with 0.607 g of 11-MUA were dissolved in 10 mL of methanol. The two solutions were mixed together and stirred overnight. After the phase transfer, the colorless hexane phase was discarded and the QDs, now in the methanol phase, were centrifuged. The precipitate was redispersed in 0.1 M KOH. The solution was washed with chloroform three times and finally redispersed in water before further use (QD-MUA).

Polymer coating of QDs: The concentration of QDs in the aqueous phase was calculated from the extinction coefficient.[86] Then, 2 mL of QD-MUA was mixed with a known QD concentration, diluted to 10 mL with water, and then centrifuged at 14 000 rcf for 20 min to remove any excess MUA in solution. The precipitate was redispersed in 2 mL of water and then mixed with 1 mL of 2 mM NaCl solution. Meanwhile, 2 mL of 1% pDADMAC solution was mixed with 1 mL of 2 mM NaCl solution under mild stirring as well. Then, the mixture with QD-MUA was added to the pDADMAC mixture dropwise under vigorous stirring. The solution was kept under vigorous stirring for 5 min and the solution was then left undisturbed for at least 1 h. After that, the solution was centrifuged at 11 000 rcf for 5 min to remove excess pDADMAC and redispersed in 2 mL water before further use.

Silica Coating on Quantum Dots: The procedure for silica coating CdSe based QDs was adopted from the previous report with minor modifications.[74] Briefly, 1.3 mL of Igepal 520 was added to 10 mL of cyclohexane and stirred for 15 min. 1 mL of 5 mg mL^{-1} quantum dots, 80 µL of tetraethoxysilane, and 150 µL 25% ammonia were added respectively with a 15 min stirring period in between each addition. After the completion of the additions, the solutions were stored in the dark for a period of time (typically about 24 h). The precipitate was collected by adding ethanol and centrifuging the solution and then rewashing with ethanol. The nanocrystals were finally redispersed in water and overcoated with pDADMAC, based on the procedure outlined earlier.

Template Patterning and EPD Cell Assembly: The template patterning and EPD cell assembly were proceed based on a previously developed method.[87,88] Differently, during the template patterning, in order to assemble nanocrystals with different sizes, the patterns on this template were designed with arrays of box cavities with sizes of 30 nm, from

50 to 310 nm (20 nm steps) and two more arrays with cavity sizes of 500 and 2000 nm. (Figure S6, Supporting Information) The center-to-center distance for each cavity was set to be 5 µm. For STED assembly, the NaCl concentration and EPD time were fixed to be 0.5 mM and 10 s for all nanocrystals. The applied potential was varied accordingly from |3| to |4| V. The potential that applied for each nanocrystal assembly was described in Table 1. Note that the fluorescence from QD arrays often exhibited quenching a few hours after assembly.

Spectroscopy: Both dark field microscopy and wide field microscopy were carried with a Nikon Lv100 Eclipse inverted microscope in reflection configuration with minor modifications. The microscope was equipped with three lenses: LU Plan Fluor 20×/0.45, LU Plan ELWD 50×/0.55 and LU Plan Fluor 100×/0.95 Nikon Lens. All spectra were recorded with a Pixis 1024F CCD camera and an Acton Micro-Spec 2150i spectrometer. Another CMOS camera (Thorlab) was used for imaging. The collected signals were analyzed with Igor software. For the dark field microscopy, a 100 W quartz halogen lamp was used as the light source. A dark field condenser was also placed in the light path to form the dark field illumination ring. For wide field microscopy, two monochromatic lasers (375 and 544 nm) were used to illuminate the sample. Two dichroic mirrors were employed to filter the light. A long pass filter was used to eliminate stray incident light. Different long pass filters were selected according to the expected emission peak of the nanocrystals. Note that it was dangerous to directly observe the wide field image through the eyepiece. It was better to use the CMOS camera for both observation and imaging.

Electron Microscopy: The TEM characterization was carried with a Tecnai F20 (FEI) TEM at 20 kV acceleration voltage. The scanning electron microscopy characterization was carried with a Nova Nanolab (FEI) SEM at 5 or 7 kV and 1.6 nA.

Atomic Force Microscopy: AFM and MFM imaging carried out using an asylum research AFM with CoCr coated silicon cantilevers (ASYMFM-R2, Oxford Instruments).

Supporting Information

Supporting Information is available from the Wiley Online Library or from the author.

Acknowledgements

The authors thank the Australian Research Council for support under grants CE170100026, LP160100054, LE110100161, and LF100100117. The authors thank the Albert Shimmins Fund for a writing up award. The authors thank the Melbourne Advanced Microscopy Facility (Bio21, The University of Melbourne) for electron microscopy access. The authors thank Dr. Tian Zheng and the Materials Characterization and Fabrication Platform (MCFP, The University of Melbourne) for their assistance with AFM/MFM characterization. This work was performed in part at the Melbourne Centre for Nanofabrication (MCN), a node of the Australian National Fabrication Facility (ANFF).

Open access publishing facilitated by The University of Melbourne, as part of the Wiley - The University of Melbourne agreement via the Council of Australian University Librarians.

Conflict of Interest

The authors declare no conflict of interest.

Data Availability Statement

The data that support the findings of this study are available from the corresponding author upon reasonable request.

Keywords

assembly methods, direct assembly, electrophoretic deposition, nanocrystals, single nanocrystal arrays

Received: January 25, 2022
Revised: April 9, 2022
Published online: May 28, 2022

[1] P. Mulvaney, *Langmuir* **1996**, *12*, 788.
[2] C. J. Orendorff, T. K. Sau, C. J. Murphy, *Small* **2006**, *2*, 636.
[3] M. Wang, L. He, W. Xu, X. Wang, Y. Yin, *Angew. Chem., Int. Ed.* **2015**, *54*, 7077.
[4] C. R. Bullen, P. Mulvaney, *Nano Lett.* **2004**, *4*, 2303.
[5] B. Zhou, B. Shi, D. Jin, X. Liu, *Nat. Nanotechnol.* **2015**, *10*, 924.
[6] J. Chen, B. Lim, E. P. Lee, Y. Xia, *Nano Today* **2009**, *4*, 81.
[7] W. Yu, M. D. Porosoff, J. G. Chen, *Chem. Rev.* **2012**, *112*, 5780.
[8] Y. Dong, B. Jia, F. Fu, H. Zhang, L. Zhang, J. Zhou, *Angew. Chem., Int. Ed.* **2016**, *55*, 13504.
[9] D. Akinwande, N. Petrone, J. Hone, *Nat. Commun.* **2014**, *5*, 5678.
[10] Y. Dong, X. Jiang, J. Mo, Y. Zhou, J. Zhou, *Chem. Eng. J.* **2020**, *381*, 122614.
[11] D. Jimenez de Aberasturi, A. B. Serrano-Montes, J. Langer, M. Henriksen-Lacey, W. J. Parak, L. M. Liz-Marzán, *Chem. Mater.* **2016**, *28*, 6779.
[12] T. D. James, P. Mulvaney, A. Roberts, *Nano Lett.* **2016**, *16*, 3817.
[13] T. Kawawaki, H. Zhang, H. Nishi, P. Mulvaney, T. Tatsuma, *J. Phys. Chem. Lett.* **2017**, *8*, 3637.
[14] Y. Dong, E. M. Akinoglu, H. Zhang, F. Maasoumi, J. Zhou, P. Mulvaney, *Adv. Funct. Mater.* **2019**, *0*, 1904290.
[15] M. Li, R. B. Bhiladvala, T. J. Morrow, J. A. Sioss, K.-K. Lew, J. M. Redwing, C. D. Keating, T. S. Mayer, *Nat. Nanotechnol.* **2008**, *3*, 88.
[16] C. Blauth, P. Mulvaney, T. Hirai, *J. Appl. Phys.* **2019**, *125*, 195501.
[17] J. Hu, D. Wang, D. Bhowmik, T. Liu, S. Deng, M. P. Knudson, X. Ao, T. W. Odom, *ACS Nano* **2019**, *13*, 4613.
[18] A. Espinosa, A. K. A. Silva, A. Sánchez-Iglesias, M. Grzelczak, C. Péchoux, K. Desboeufs, L. M. Liz-Marzán, C. Wilhelm, *Adv. Healthcare Mater.* **2016**, *5*, 1040.
[19] W.-J. Joo, J. Kyoung, M. Esfandyarpour, S.-H. Lee, H. Koo, S. Song, Y.-N. Kwon, S. H. Song, J. C. Bae, A. Jo, M.-J. Kwon, S. H. Han, S.-H. Kim, S. Hwang, M. L. Brongersma, *Science* **2020**, *370*, 459.
[20] S. Kusumoputro, S. Tseng, J. Tse, C. Au, C. Lau, X. Wang, T. Xia, *View* **2020**, *1*, 20200105.
[21] R. Medhi, P. Srinoi, N. Ngo, H.-V. Tran, T. R. Lee, *ACS Appl. Nano Mater.* **2020**, *3*, 8557.
[22] M. A. Boles, M. Engel, D. V. Talapin, *Chem. Rev.* **2016**, *116*, 11220.
[23] I. Pastoriza-Santos, C. Kinnear, J. Pérez-Juste, P. Mulvaney, L. M. Liz-Marzán, *Nat. Rev. Mater.* **2018**, *3*, 375.
[24] S. Zhang, C. I. Pelligra, X. Feng, C. O. Osuji, *Adv. Mater.* **2018**, *30*, 1705794.
[25] H. Zhang, C. Kinnear, P. Mulvaney, *Adv. Mater.* **2020**, *32*, 1904551.
[26] E. V. Shevchenko, D. V. Talapin, N. A. Kotov, S. O'Brien, C. B. Murray, *Nature* **2006**, *439*, 55.
[27] M. A. Boles, M. Engel, D. V. Talapin, *Chem. Rev.* **2016**, *116*, 11220.
[28] R. Iida, H. Mitomo, K. Niikura, Y. Matsuo, K. Ijiro, *Small* **2018**, *14*, 1704230.
[29] X. Zhou, Y. Zhou, J. C. Ku, C. Zhang, C. A. Mirkin, *ACS Nano* **2014**, *8*, 1511.
[30] C. Kuemin, L. Nowack, L. Bozano, N. D. Spencer, H. Wolf, *Adv. Funct. Mater.* **2012**, *22*, 702.
[31] C. Kuemin, R. Stutz, N. D. Spencer, H. Wolf, *Langmuir* **2011**, *27*, 6305.

[32] M. Asbahi, S. Mehraeen, F. Wang, N. Yakovlev, K. S. L. Chong, J. Cao, M. C. Tan, J. K. W. Yang, *Nano Lett.* **2015**, *15*, 6066.
[33] V. Flauraud, M. Mastrangeli, G. D. Bernasconi, J. Butet, D. T. Alexander, E. Shahrabi, O. J. Martin, J. Brugger, *Nat. Nanotechnol.* **2017**, *12*, 73.
[34] S. Kang, T. Kim, S. Cho, Y. Lee, A. Choe, B. Walker, S.-J. Ko, J. Y. Kim, H. Ko, *Nano Lett.* **2015**, *15*, 7933.
[35] C. Kinnear, J. Cadusch, H. Zhang, J. Lu, T. D. James, A. Roberts, P. Mulvaney, *Langmuir* **2018**, *34*, 7355.
[36] L. Teulon, Y. Hallez, S. Raffy, F. Guerin, E. Palleau, L. Ressier, *J. Phys. Chem. C* **2019**, *123*, 783.
[37] D. Morales, L. Teulon, E. Palleau, T. Alnasser, L. Ressier, *Langmuir* **2018**, *34*, 1557.
[38] D. Nepal, M. S. Onses, K. Park, M. Jespersen, C. J. Thode, P. F. Nealey, R. A. Vaia, *ACS Nano* **2012**, *6*, 5693.
[39] K. R. Gadelrab, Y. Ding, R. Pablo-Pedro, H. Chen, K. W. Gotrik, D. G. Tempel, C. A. Ross, A. Alexander-Katz, *Nano Lett.* **2018**, *18*, 3766.
[40] S. Nedev, A. S. Urban, A. A. Lutich, J. Feldmann, *Nano Lett.* **2011**, *11*, 5066.
[41] J. Do, M. Fedoruk, F. Jäckel, J. Feldmann, *Nano Lett.* **2013**, *13*, 4164.
[42] A. S. Urban, A. A. Lutich, F. D. Stefani, J. Feldmann, *Nano Lett.* **2010**, *10*, 4794.
[43] B. D. Myers, E. Palacios, D. I. Myers, S. Butun, K. Aydin, V. P. Dravid, *Nano Lett.* **2019**, *19*, 4535.
[44] N. Liu, T. Liedl, *Chem. Rev.* **2018**, *118*, 3032.
[45] Q.-Y. Lin, J. A. Mason, Z. Li, W. Zhou, M. N. O'brien, K. A. Brown, M. R. Jones, S. Butun, B. Lee, V. P. Dravid, *Science* **2018**, *359*, 669.
[46] Y. Yin, Y. Lu, B. Gates, Y. Xia, *J. Am. Chem. Soc.* **2001**, *123*, 8718.
[47] C. Hanske, M. Tebbe, C. Kuttner, V. Bieber, V. V. Tsukruk, M. Chanana, T. A. F. König, A. Fery, *Nano Lett.* **2014**, *14*, 6863.
[48] L. Besra, M. Liu, *Progress Mater. Sci.* **2007**, *52*, 1.
[49] O. O. Van der Biest, L. J. Vandeperre, *Annu. Rev. Mater. Sci.* **1999**, *29*, 327.
[50] M. Giersig, P. Mulvaney, *J. Phys. Chem.* **1993**, *97*, 6334.
[51] J. H. Dickerson, A. R. Boccaccini, *Electrophoretic Deposition of Nanomaterials*, Springer, Berlin, Heidelberg **2011**.
[52] A. Singh, N. J. English, K. M. Ryan, *J. Phys. Chem. B* **2012**, *117*, 1608.
[53] K. W. Song, R. Costi, V. Bulović, *Adv. Mater.* **2013**, *25*, 1420.
[54] A. Salant, M. Shalom, I. Hod, A. Faust, A. Zaban, U. Banin, *ACS Nano* **2010**, *4*, 5962.
[55] S. J. An, Y. Zhu, S. H. Lee, M. D. Stoller, T. Emilsson, S. Park, A. Velamakanni, J. An, R. S. Ruoff, *J. Phys. Chem. Lett.* **2010**, *1*, 1259.
[56] C. Du, N. Pan, *Nanotechnology* **2006**, *17*, 5314.
[57] D. V. Bavykin, L. Passoni, F. C. Walsh, *Chem. Commun.* **2013**, *49*, 7007.
[58] S. Mahajan, J. Dickerson, *Nanotechnology* **2010**, *21*, 145704.
[59] E. M. Wong, P. C. Searson, *Appl. Phys. Lett.* **1999**, *74*, 2939.
[60] T. Kraus, L. Malaquin, H. Schmid, W. Riess, N. D. Spencer, H. Wolf, *Nat. Nanotechnol.* **2007**, *2*, 570.
[61] L. Malaquin, T. Kraus, H. Schmid, E. Delamarche, H. Wolf, *Langmuir* **2007**, *23*, 11513.
[62] K. D. Barbee, A. P. Hsiao, M. J. Heller, X. Huang, *Lab Chip* **2009**, *9*, 3268.
[63] F. Qian, A. J. Pascall, M. Bora, T. Y.-J. Han, S. Guo, S. S. Ly, M. A. Worsley, J. D. Kuntz, T. Y. Olson, *Langmuir* **2015**, *31*, 3563.
[64] A. A. Shah, M. Ganesan, J. Jocz, M. J. Solomon, *ACS Nano* **2014**, *8*, 8095.
[65] A. A. Shah, H. Kang, K. L. Kohlstedt, K. H. Ahn, S. C. Glotzer, C. W. Monroe, M. J. Solomon, *Small* **2012**, *8*, 1551.
[66] J. Gao, X. Ran, C. Shi, H. Cheng, T. Cheng, Y. Su, *Nanoscale* **2013**, *5*, 7026.
[67] W. Fudickar, T. Linker, *J. Am. Chem. Soc.* **2012**, *134*, 15071.
[68] J. Mei, N. L. C. Leung, R. T. K. Kwok, J. W. Y. Lam, B. Z. Tang, *Chem. Rev.* **2015**, *115*, 11718.
[69] J. M. Hodgkiss, S. Albert-Seifried, A. Rao, A. J. Barker, A. R. Campbell, R. A. Marsh, R. H. Friend, *Adv. Funct. Mater.* **2012**, *22*, 1567.
[70] M. Mitsui, Y. Kawano, R. Takahashi, H. Fukui, *RSC Adv.* **2012**, *2*, 9921.
[71] K. Boldt, N. Kirkwood, G. A. Beane, P. Mulvaney, *Chem. Mater.* **2013**, *25*, 4731.
[72] K. S. Mayya, B. Schoeler, F. Caruso, *Adv. Funct. Mater.* **2003**, *13*, 183.
[73] L. M. Liz-Marzán, M. Giersig, P. Mulvaney, *Langmuir* **1996**, *12*, 4329.
[74] F. Pietra, R. J. A. van Dijk Moes, X. Ke, S. Bals, G. Van Tendeloo, C. de Mello Donega, D. Vanmaekelbergh, *Chem. Mater.* **2013**, *25*, 3427.
[75] F. Strubbe, F. Beunis, T. Brans, M. Karvar, W. Woestenborghs, K. Neyts, *Phys. Rev. X* **2013**, *3*, 021001.
[76] H. Ohshima, T. W. Healy, L. R. White, *J. Colloid Interface Sci.* **1982**, *90*, 17.
[77] R. J. Hunter, *Zeta Potential in Colloid Science: Principles and Applications*, Vol. 2, Academic Press, New York **2013**.
[78] M. von Smoluchowski, *Z. Phys. Chem* **1917**, *92*, 129.
[79] R. W. O'Brien, L. R. White, *J. Chem. Soc., Faraday Trans.* **1978**, *74*, 1607.
[80] X. Ye, C. Zheng, J. Chen, Y. Gao, C. B. Murray, *Nano Lett.* **2013**, *13*, 765.
[81] H.-Y. Ahn, H.-E. Lee, K. Jin, K. T. Nam, *J. Mater. Chem. C* **2013**, *1*, 6861.
[82] C. Li, K. L. Shuford, M. Chen, E. J. Lee, S. O. Cho, *ACS Nano* **2008**, *2*, 1760.
[83] N. G. Bastús, J. Comenge, V. Puntes, *Langmuir* **2011**, *27*, 11098.
[84] W. K. Bae, M. K. Nam, K. Char, S. Lee, *Chem. Mater.* **2008**, *20*, 5307.
[85] T. Kodanek, H. M. Banbela, S. Naskar, P. Adel, N. C. Bigall, D. Dorfs, *Nanoscale* **2015**, *7*, 19300.
[86] J. Jasieniak, L. Smith, J. van Embden, P. Mulvaney, M. Califano, *J. Phys. Chem. C* **2009**, *113*, 19468.
[87] H. Zhang, J. Cadusch, C. Kinnear, T. James, A. Roberts, P. Mulvaney, *ACS Nano* **2018**, *12*, 7529.
[88] H. Zhang, Y. Liu, M. F. S. Shahidan, C. Kinnear, F. Maasoumi, J. Cadusch, E. M. Akinoglu, T. D. James, A. Widmer-Cooper, A. Roberts, P. Mulvaney, *Adv. Funct. Mater.* **2021**, *31*, 2006753.